Intracellular dynamics of CA3 pyramidal cells supporting sparse coding during theta and large irregular activity

Meryl Malezieux[1,2]*, Ashley L. Kees[1,2]* and Christophe Mulle[1,2,3]

[1]Interdisciplinary Institute for Neuroscience, CNRS UMR 5297

[2]University of Bordeaux, F-33000 Bordeaux, France

**equal contribution*

[3]Lead contact; correspondence: christophe.mulle@u-bordeaux.fr

Abstract

The hippocampal local field potential (LFP) displays large irregular activity (LIA) during quiet wakefulness and theta oscillations during exploratory behaviors. The hippocampal CA3 subregion is important for rapid memory encoding and integrates multimodal information processed in the entorhinal cortex. We have explored the intracellular dynamics of CA3 pyramidal cells (PCs) in awake mice using whole-cell and LFP recordings in awake head-fixed mice combined with measurements of pupil diameter and running speed. We have examined how single properties contribute to network processing across brain states. LIA coincides with higher synaptic and network noise and in some cells, starts with a transient increase in Vm and firing. During theta, most CA3 PCs hyperpolarize, reduce firing, and have lower Vm variance. However, a small subpopulation of CA3 PCs depolarizes and increases firing. These intracellular modulations during theta and LIA allow sparse coding in CA3 across different brain states.

Introduction

Wakefulness is comprised of distinct brain states, correlated with different behaviors and characterized by specific oscillatory patterns in the local field potential (LFP). The ability of brain circuits to generate distinct brain states and oscillations is thought to rely upon modulations in single-cell properties, such as resting membrane potential, spike threshold, and synaptic efficacy (Marder et al., 2014). Monitoring the membrane potential of individual neurons *in vivo* is therefore essential to understand how single-cell properties contribute to network processing across different brain states.

The hippocampus plays a critical role in the encoding, consolidation and retrieval of episodic memories, which combine both spatial and non-spatial information (Buzsáki and Moser, 2013; Eichenbaum, 2016). Oscillatory dynamics and the firing patterns of neural ensembles in the hippocampus support spatial coding as demonstrated by a large number of studies based on extracellular recordings in freely behaving animals (Buzsáki and Moser, 2013). During wakefulness, periods of locomotion are associated with robust theta (4–12 Hz) and gamma (30–80 Hz) oscillations in the LFP. Since their discovery in the rabbit hippocampus, theta rhythms have been extensively studied and found in many species including rats, mice, monkeys and humans (Ekstrom et al., 2005; Green and Arduini, 1954; Jutras et al., 2013; Vanderwolf, 1969). The percentage of time in which theta is present in the LFP can predict the rate of acquisition and the quality of a memory, suggesting an important role for theta in the formation of memories (Berry and Thompson, 1978; Gupta et al., 2012; Landfield et al., 1972; Mizuseki et al., 2009). Additionally, theta correlates with behaviors associated with active sampling of the environment, like exploring, sniffing and whisking, and therefore appears well suited for the coordination of multimodal sensory integration (Komisaruk, 1970; Macrides et al., 1982). During non-locomotor behaviors, such as immobility, eating, drinking, and grooming, as well as during slow wave sleep, large irregular activity (LIA) can be detected in the hippocampal LFP. The LIA pattern is marked by high-amplitude broadband fluctuations rather than oscillations at a specific frequency band and is often characterized by the presence of sharp-waves (50 ms duration) that co-occur with high-frequency ripple oscillations (80-250 Hz) (SWRs) (Buzsáki, 1986; O'Keefe, 1976; Vanderwolf, 1969). LIA is present during periods of low arousal and is thought to represent a state in which memory consolidation and retrieval of episodic memory is promoted (Buzsáki, 2015; Carr et al., 2011).

Intracellular activity from single CA1 pyramidal cells (PCs) in awake behaving animals has provided unprecedented insight into the relationship between network and single-cell activity and its role in behavior and cognition. The combination of intracellular and multisite extracellular recordings *in vivo* in awake rodents has allowed characterizing membrane potential dynamics to reveal synaptic mechanisms of CA1 PCs SWRs (English et al., 2014; Gan et al., 2017; Hulse et al., 2016; Maier et al., 2011) and in relation to brain state and arousal (Hulse et al., 2017). CA1 hippocampal place cells have been recorded intracellularly in both freely moving (Epsztein et al., 2011) and head-fixed (Bittner et al., 2015; Cohen et al., 2017; Harvey, et al., 2009) rodents, enabling the direct measurement and manipulation of inputs and cell-intrinsic properties during spatial exploration. For example, recordings of subthreshold events have led to the hypothesis that a nonlinear interaction between inputs from the entorhinal cortex (EC) and CA3 allows the CA1 circuit to associate contextual and spatial information (Bittner et al., 2015; Grienberger et al., 2014).

Within the hippocampus, these types of studies have been mostly restricted to CA1, and the few studies that have examined the intracellular activity of CA3 PCs *in vivo* have been performed in anesthetized rats (Kowalski et al., 2016) and mice (Zucca et al., 2017). CA3, the main excitatory input to CA1, is unique in both its anatomical and functional characteristics; CA3 PCs display extensive recurrent connections, and receive strong mossy fiber input from dentate granule cells (Rebola et al., 2017). Computational theories have long proposed that CA3 rapidly stores memories through synaptic plasticity in the autoassociative

network formed by its recurrent connections (Kesner and Rolls, 2015), and CA3 is indeed necessary for one-trial memory encoding (Nakazawa et al., 2003). Moreover, experimental evidence and theory support that efficient episodic memory representations require a sparsely distributed neural code, in which each memory is coded by the activity of a small proportion of hippocampal neurons (Leutgeb et al., 2007; Marr, 1971; Wixted et al., 2014). Considering the importance of CA3 in rapid encoding and retrieval of episodic memories, we hypothesized that intracellular properties of CA3 PCs adapt to state-dependent network changes to ensure sparse coding. We have thus explored the modulation of intracellular dynamics of CA3 PCs during changes in brain state by using whole-cell patch-clamp and LFP recordings in awake head-fixed mice in combination with measurements of pupil diameter and running activity on a wheel.

We report that during theta, most CA3 PCs are silenced by membrane potential hyperpolarization while only a small subpopulation is activated through depolarization. On the other hand, LIA is associated with a general decrease in excitability of CA3 PCs despite higher membrane potential fluctuations, with only a few cells showing consistent but transient depolarizations and increase in excitability at transitions to LIA. Altogether, we show that different single-cell modulations are taking place during theta and LIA, all of them ensuring that only a few cells are active while the others are silent during both states, therefore supporting sparse coding in the population across different network regimes and brain states.

Results

Hippocampal CA3 LFP characterization and brain state classification

To investigate the intracellular dynamics of CA3 PCs *in vivo* across brain states, we performed simultaneous whole-cell and LFP recordings in awake head-fixed mice free to run on a wheel (Figure 1A). An LFP electrode was first positioned in the *stratum pyramidale* of CA3 before lowering the patch-clamp electrode for whole-cell recordings in the vicinity of the LFP electrode. We aimed to position the tips of the LFP and patch electrodes within 200 µm of each other; electrode positions were confirmed post-hoc by histology. Pyramidal cell identity was determined by the voltage response to current steps as well as by the presence of spontaneous or evoked burst firing (Figure 1B and 1C). To monitor the level of arousal, we measured both pupil diameter and locomotor activity on the wheel (Figures 1A and 1C). Figure 1C shows an example of a simultaneous current-clamp recording from a CA3 PC aligned with the corresponding LFP recording, locomotor activity and pupil diameter. We recorded a total of 35 CA3 PCs. In some cases, the patched cell was filled with biocytin and recovered in histology, confirming the cell identity (Figure 1D), and in all cases, the patch pipette position was confirmed to have been in CA3. The basic properties of each CA3 PC recorded are shown in Tables S1 and S2.

Brain state classification was achieved offline using the spectrogram of the LFP to find epochs of theta and LIA (Figures 2A and 2B). Theta was detected using the ratio of power in the theta (6-9 Hz) range to power in the delta (0.5-3 Hz) range (Figure 2B). From a total of 890 theta events detected from all recordings, 58% occurred in conjunction with detected locomotor activity (run theta); the remaining 42% were categorized as rest theta. LIA was detected as peaks in the average broadband power (0.5-80 Hz) after z-scoring within frequency bands; events that overlapped with theta events were not included (Figure 2B). Theta and LIA events were dispersed throughout the session with no apparent pattern (Figure 2C). Over a total recording time of 270 minutes, 15% was classified as run theta, 6% as rest theta, and 10% as LIA, leaving 69% unlabeled (Figure 2F). Out of the three event types, run theta occurred for the longest duration (Figure 2D). Both types of theta events occurred significantly more often than LIA (Figure 2E). The pupil diameter of the mice was smaller during LIA as compared to theta (Figures 2G and S2). This is consistent with previous reports (Hulse et al., 2017), and provides an independent confirmation of the criteria used in the detection of brain states. Interestingly, the theta-delta ratio was significantly higher during run theta than rest theta (Figure 2H). For run theta events, increases in the theta-delta ratio often

preceded the start of the detected run (Figure 2I), which has also been noted in previous studies (Fuhrmann et al., 2015; Green and Arduini, 1954; Vanderwolf, 1969). Thus, we were able to detect theta and LIA events using the LFP positioned in the CA3 *stratum pyramidale* and we could characterize the intracellular dynamics of nearby CA3 PCs in relation to these brain states.

Most CA3 PCs hyperpolarize during theta

We explored the membrane potential of CA3 PCs in relation to theta (Figure 3), a brain state during which spatial and episodic memory encoding is thought to preferentially occur. We hypothesized that during this state, the properties of CA3 PCs would be optimal for the integration of incoming multimodal information from the DG and EC. We performed our analyses on smoothed and downsampled membrane potential traces after spike removal (Figure S1A). We observed that the membrane potential decreased at the onset of the theta in a large proportion of events (Figure 3A). While the average trace at the onset of all theta events showed a hyperpolarization, individual theta events could be accompanied by hyperpolarization, depolarization, or no significant change (Figure 3B). Out of the 848 theta events in which the membrane potential could be reliably recorded, 46% were associated with a significant hyperpolarization, 26% with depolarization and 28% showed no significant modulation (Figure 3C). Compared with randomly-selected times, there was a significantly higher proportion of hyperpolarizing events and significantly lower proportion of depolarizing and nonsignificant events, suggesting not only that the membrane potential tends to change at the onset of theta, but that this change tends to be a hyperpolarization. In addition, the duration of hyperpolarization was closely correlated with the duration of the theta event (Figure S3A). We observed no difference in the magnitude or proportion of modulation between run theta and rest theta, suggesting that the relationship between theta and membrane potential does not depend on the running behavior, but is more closely related to the internal brain state (Figure 3D). We observed that while many cells consistently hyperpolarized during theta, a few cells consistently depolarized, and several cells sometimes displayed a mixed behavior of both depolarizations and hyperpolarizations. To identify the cells that displayed a consistent modulation, we shuffled the data for each cell by shifting the time relationship between the membrane potential trace and theta events; cells that showed a larger positive or negative average change than was observed in the shuffled data were considered significantly depolarizing or hyperpolarizing, respectively. By this measure, 16 cells were significantly hyperpolarizing during theta, 3 were significantly depolarizing, and 16 showed no difference with the shuffled data set, perhaps due to a variable change in Vm at the onset of theta events (Figure 3E).

LIA is associated with depolarization of CA3 PCs

We performed similar analyses looking at the intracellular properties of CA3 PCs during LIA (Figure 4A), a brain state characterized by the presence of SWRs, which have been shown to play a role in memory consolidation. We hypothesized that in this brain state, the properties of individual CA3 PCs should favor integration of recurrent inputs from other CA3 PCs. Indeed, during LIA events, the membrane potential of CA3 PCs tended to depolarize, suggesting that they entered a more excitable state, possibly supporting the generation of SWRs (Figure 4B). It is worth noting that the depolarization tended to start before the onset of LIA and end after a few seconds, regardless of the length of the LIA state (Figure S3B). As with theta events, the response was heterogeneous, with some LIA events coinciding with a depolarization, hyperpolarization, or no significant change in the membrane potential (Figure 4B). Out of 426 LIA events, 44% were associated with a depolarization, 19% with a hyperpolarization, and 37% with no change, which represents more depolarizations and fewer hyperpolarizations than would be expected by chance (Figure 4C). However, when comparing each cell's modulations with those from shifted time series, only 8 cells consistently depolarized, 2 cells consistently hyperpolarized, and 24 cells showed no consistent modulation (in one cell, no LIA events were recorded) (Figure 4D). Although LIA events are associated with a high proportion of depolarizations, it seems that those depolarizations happen throughout the cell

population and not specifically in a subset of cells. Therefore, many cells have a variety of responses to different LIA events, in line with recent research showing different ensembles are active during different SWRs (Ramirez-Villegas et al., 2015; Taxidis et al., 2015). Of the 8 LIA-depolarizing cells, 7 were also theta-hyperpolarizing, suggesting that this is a common combination of responses and that there is considerable overlap between cells that are consistently modulated by either brain state (Figure 4E, Table S1). We also examined whether the cells active during theta consistently reactivated during LIA, but we did not find evidence for this in our small population of theta-depolarizing cells (Table S1).

Dynamic regulation of action potential threshold during theta and LIA

Having seen a direct modulation of the membrane potential of CA3 PCs during theta and LIA, we asked if these modulations have an impact on the firing properties, and therefore the output, of the cell. Cells that had a significant change in membrane potential for either brain state had a corresponding change in average firing rate (Figure S4). To determine the mechanisms underlying the state-dependent changes in firing, we looked at the firing threshold relative to the ongoing membrane potential. Spiking threshold varies dynamically depending on a variety of factors (Azouz and Gray, 2003; Epsztein et al., 2011) (Figure S1C) and the distance between the membrane potential and spike threshold influences the amount of coincident input necessary to elicit a spike. The relationship between the membrane potential and spike threshold could differ between theta and LIA to preserve sparse coding during the two states. We measured this relationship by detecting the threshold potential of each spike and subtracting it from the average membrane potential calculated from a window between 500 and 50 ms preceding the spike (Figures 5A and S1B). Because the spike threshold is modulated within bursts, care was taken to use only the spikes with a prior inter-spike interval of at least 50 ms. Overall, the distance to spike threshold is increased during LIA (Figure 5B). This result was surprising since we show that the transition to LIA is mainly associated with depolarizations (Figure 4). To explore further, we separated spikes depending on the state and associated membrane potential modulation. We then made spike-triggered averages of the membrane potential relative to threshold for the respective groups (Figure 5C). The averages looked similar for spikes that occurred during theta, regardless of the change in membrane potential (Figure 5C, left panel). However, intracellular theta oscillations are apparent in the spike-triggered average traces, suggesting that spikes occur at a similar phase of theta. The average traces for LIA show that, consistent with Figure 5B, there is an increased distance between membrane potential and spike threshold during events associated with a hyperpolarization or no change (Figure 5C, right panel, blue and grey traces). However, for spikes occurring during a window corresponding to the peak of LIA depolarizations, the relative membrane potential was similar to that for all spikes (Figure 5C, right panel, red and black traces). This suggests that while the distance between membrane potential and spike threshold is increased during LIA, depolarizations are capable of momentarily decreasing this distance.

To illustrate this fast change in distance to spike threshold, Figures 5D and 5E show the short time-scale dynamics of firing properties around significant hyperpolarizations and depolarizations at the starts of theta and LIA. Around theta onsets, hyperpolarizations are associated with a decrease in firing rate but no change in the distance to spike threshold (Figures 5D and 5F, left panel). However, depolarizations are associated with an increase in firing rate accompanied by a reduced distance to threshold (Figures 5E and 5F, left panel). This suggests that depolarizations occurring during theta are increasing the cells' excitability to facilitate an increase in firing rate.

Just as in theta, transitions to LIA are associated with a change in firing rate that closely matches the change in membrane potential (Figures 5D-F, right panels). In this state, both hyperpolarizations and depolarizations are effective in causing a significant change in the distance to spike threshold. This change is brief and occurs partially before the start of detected LIA. Altogether, we conclude that during LIA, the membrane potential of CA3 PCs is usually further away from spike threshold making cells less

excitable. However, during the onset of the state, there is a transient increase in membrane potential for some cells, bringing them closer to firing threshold and inducing an increase in firing rate. The general increase in the firing threshold relative to membrane potential may be important during LIA to ensure that only the selected depolarizing cells increase their firing rate.

Interestingly, the fast changes in distance to threshold were on average smaller during periods that were not already classified as either theta or LIA than those seen during these states (Figure S5). We observed no evidence of short-timescale state-dependent changes in the distance to firing threshold over a shorter window (25-15 ms prior to spike initiation) (Figure S6). This measure is equivalent to the slope of the pre-spike depolarization, which has previously been shown to be independent of brain state (Poulet and Petersen, 2008).

Possible mechanisms of intracellular modulation in CA3 PCs during different brain states

To provide a mechanistic explanation for the modulation of Vm observed during theta and LIA, we examined the correlation between the change in membrane potential and the initial membrane potential before the state transition (Figure 6). To exclude the possible influence of the holding current imposed on the cell membrane, we restricted this analysis to events when less than 10 pA holding current was injected through the patch pipette. During theta events, the initial membrane potential was significantly correlated with the change in membrane potential, suggesting that the direction of the modulation during theta depends on changes in driving force (Figure 6A, left panel). To validate this hypothesis, we injected hyperpolarizing current into the cells through the patch pipette to reverse the driving force. Contrary to our expectations, this manipulation did not increase the proportion of depolarizing events, but rather led to an insignificant increase in the proportion of hyperpolarizing theta events (Figure 6A, right panel). This may in part be due to the difficulty in controlling the resting membrane potential of cells *in vivo*, and of remote compartments in particular (Spruston et al., 1993). Another possible explanation is that the changes occurring during theta are more complex than just a change in the conductance of a single ion species. In contrast, during LIA, the change in membrane potential was only slightly correlated with the initial value (Figure 6B, left panel), suggesting that the driving force alone cannot account for the variability in membrane potential modulation. Unsurprisingly, manipulations of the membrane potential with current injections did not significantly alter the proportion of hyperpolarizing and depolarizing events associated with LIA (Figure 6B, right panel).

To further test whether the membrane potential changes were due to modulations in the activity of ion channels, we measured the input resistance in a separate set of 13 cells during theta and LIA. When we directly compared the input resistance measurements taken during theta and LIA, 7 out of 13 cells showed a small but significantly higher input resistance during LIA as compared to theta (Figure S7). A difference in input resistance between the two brain states could reflect different intrinsic properties for synaptic integration and spiking output.

To explore the possibility that state-dependent membrane potential modulations could be correlated with properties of the network either during or immediately preceding the state, we prepared average spectrograms of the LFP triggered by the start of theta or LIA, keeping events separated depending on the direction of membrane potential modulation in the recorded cell (Figure S8). We did not observe any obvious differences in the spectral components of the LFP between the different event types, consistent with the hypothesis that the direction of modulation is controlled individually within cells, rather than globally in the whole network.

As a proxy for changes in synaptic activity, we analyzed the synaptic noise by measuring the variance of the membrane potential during LIA and theta (Figure 7). The term synaptic noise refers to the irregular

membrane potential fluctuations of neurons *in vivo,* which are caused by the discharge of presynaptic neurons. Figure 7A shows an example of the membrane potential of a cell after spike removal (top black trace) and smoothing (grey trace). The residual trace was calculated by taking the difference between the spike-removed and smoothed traces; the variance was measured from this trace in sliding windows of 1 second. In comparison to all other times, the variance was significantly higher during LIA and significantly lower during theta (Figure 7B). This relationship does not seem to depend on whether the cells hyperpolarize or depolarize; that is, theta-depolarizing cells also have reduced variance during theta, and LIA-hyperpolarizing cells have increased variance during LIA. This is important to note because the variance tends to be correlated with the average membrane potential. This led us to ask whether the brain state can influence the normal relationship between Vm and variance. To do this analysis, we first identified all the significant hyperpolarizing and depolarizing events, and separated them based on whether they coincided with the onset of theta or LIA. The average traces of membrane potential and variance for all hyperpolarizations and depolarizations are shown in Figures 7C and 7D, respectively. The variance was then taken at the end of each hyperpolarization or depolarization. Variance was lower during theta-associated than LIA-associated hyperpolarizations (Figure 7C), and the same was true of depolarizations (Figure 7D). Taken together, these results suggest that the reduction in variance that occurs during theta is not merely a byproduct of the change in membrane potential and that a specific mechanism is taking place to reduce variance during theta. Similarly, LIA is accompanied with an increase in variance in addition to what would normally occur with a depolarization.

Increased synaptic input from GABAergic interneurons would favor hyperpolarization, with an initial increase in synaptic noise followed by a decrease as the cell membrane approaches the reversal potential for chloride. We indeed found a nonzero delay between hyperpolarization of the membrane potential and changes in variance, but this was not state-dependent (Figure S9).

Discussion

Modulations in single-cell properties, such as resting membrane potential, intrinsic excitability and synaptic activity are thought to underlie the ability of brain circuits to generate the activity patterns that correlate with distinct brain states (Marder et al., 2014). Of importance is the ability to maintain sparse coding despite the large network changes that occur between these states. In the neocortex, recordings of single cell membrane potential dynamics across brain states and during behavior have been key in elucidating the cellular mechanisms underlying the occurrence of distinct network activity patterns (Crochet and Petersen, 2006; Polack et al., 2013; Schneider et al., 2014). In the hippocampus of awake behaving rodents, modulation of the activity of neural ensembles and network oscillations has been extensively studied, especially regarding spatial information processing (Buzsáki and Moser, 2013). Here we have examined the intracellular mechanisms of CA3 cells underlying the emergence of network activity patterns in the awake animal across brain states and we propose mechanisms by which the modulation of neuronal properties supports sparse coding in this hippocampal subregion during different network regimes.

During active behaviors such as running, hippocampal pyramidal cells are engaged in encoding and recall of information, requiring that certain cells are active while others are silent. Within a given environment, only a portion of the PCs will be involved in the neural representation. We provide evidence for this, as over the population, CA3 PCs were more likely to hyperpolarize and decrease their firing during theta, and only 3 of the 35 CA3 PCs recorded were consistently activated during theta. These results did not depend on whether the theta event overlapped with detected running, suggesting they are related to the state of the hippocampal network rather than to the behavioral output of the animal. Moreover, the duration of the

hyperpolarizations closely matches the total duration of the theta events, suggesting a tight temporal coupling between the underlying mechanism and the theta state.

We observed a decrease in the variance of the membrane potential fluctuations in CA3 PCs regardless of the change in membrane potential, a slight decrease in cell input resistance, and a dependence on the driving force, all of which point to a global increase in inhibition. However, we cannot pinpoint whether this apparent increase in inhibition is due to neuromodulation (Polack et al., 2013) or synaptic inhibitory inputs, nor can we definitively exclude other mechanisms for hyperpolarization, such as a decrease in excitatory input. We hypothesize that an initial increase in inhibition leads to the hyperpolarization and decrease in membrane fluctuations in most CA3 PCs, and that these modulations persist due to the subsequent decrease in excitatory inputs from other CA3 PCs. For the few cells that are consistently activated during theta, how they manage to increase their firing on a so-proposed background of global inhibition remains difficult to explain. Nevertheless, we have observed a robust phenomenon in intracellular dynamics that selects a few cells and excludes others from the representation, thus ensuring a high signal-to-noise ratio in the population firing.

In contrast to our results, it has been reported that CA1 PCs recorded in similar conditions display no marked modulation of membrane potential during theta (Hulse et al., 2017). However, optical recording of CA1 PCs using voltage sensitive dyes shows a decrease in firing rate and in the power of subthreshold fluctuations during walking, a behavioral state associated with theta oscillations in the hippocampus (Adam et al., 2019). This modulation of CA1 PCs occurs together with increased activity of SST interneurons, possibly driven by the medial septum (Adam et al., 2019). It is possible that a similar mechanism is taking place in the CA3 network during theta and contributes to the modulations we report.

During LIA, the brain is in a low-arousal state and instead of coding incoming sensory information, hippocampal pyramidal cells engage in offline replay of sequences associated with previously learned information. Despite the changes in the network, sparse coding is no less important here, with cells firing in precisely ordered ensembles (Foster and Wilson, 2006; Lee and Wilson, 2002). A detailed analysis of membrane potential fluctuations in CA1 PCs and in DG cells across transitions to LIA was recently made in awake head-fixed mice (Hulse et al., 2017). Most cells in both CA1 and DG depolarized and their membrane potential demonstrated increased variance. We observed similar features for CA3 PCs, although to a lesser extent. Thus, we conclude that during LIA, the intracellular properties of the principal hippocampal subtypes are biased toward the transfer of information along the hippocampal trisynaptic pathway, possibly linked to a propensity to generate and transfer SWRs which are important for memory consolidation (Buzsáki, 2015; Foster and Wilson, 2006). It should be noted that while the population of CA3 PCs tended to depolarize, 24 out of 34 cells did not do so consistently; many of these displayed a variable change in membrane potential. However, this fits well with the finding that there are different types of SWRs, each associated with the activation of a different ensemble (Ramirez-Villegas et al., 2015; Taxidis et al., 2015). This suggests that single cells could be differentially modulated during consecutive LIA events depending on the nature of the SWR contained therein. This mechanism could account for the event-by-event heterogeneity in membrane potential modulation that we observed during LIA. The increased membrane potential variance in CA3 PCs and known depolarization in upstream DG suggests that CA3 PCs experience an increase in excitatory input during LIA, but the overall increase in the distance between membrane potential and spike threshold may be a counteractive mechanism to prevent over excitation in the network. Due to this, only the select cells that depolarize increase their firing due to a temporary decrease in the distance to spike threshold. During LIA, sparse activity of the cells is therefore preserved.

In neocortical neurons, membrane potential and variance are proposed to exhibit a U-shaped dependence on arousal; compared with low-arousal states, cells are hyperpolarized during intermediate arousal, and

depolarized during phasic or tonic periods of hyper-arousal, which include periods of locomotion (McGinley et al., 2015). A similar relationship in CA1 PCs was recently proposed (Hulse et al., 2017). To determine whether the dependence on arousal for CA3 PC membrane potential is U-shaped, binary or sigmoid, we would need to detect a level of arousal intermediate to the low-arousal state of LIA and the high-arousal state of theta. One intermediate state that is present in the hippocampus is small irregular activity (SIA) (Jarosiewicz and Skaggs, 2004), noticeable in the LFP by a marked decrease in total power. SIA is present in the hippocampus of rats during transitions in alertness during immobility, such as an abrupt halt after voluntary movement (Whishaw and Vanderwolf, 1971). During SIA, pyramidal cells in CA1 and CA2, but not CA3, code for position despite the absence of locomotion (Jarosiewicz et al., 2002; Kay et al., 2016). This may suggest that SIA in CA3 could have a specific impact on CA3 PCs. However, we were not able to confidently detect SIA events in our data. In our LFP recordings from CA3 *stratum pyramidale*, decreases in total power were slight, making putative SIA events difficult to detect. Moreover, we found that even the periods of the lowest total power were not accompanied by pupil dilation, a known correlate of SIA (Hulse et al., 2016). This might be inherent to our experimental configuration, where we record the LFP at only one site adjacent to the patched cell, preventing us from comparing across different CA3 layers that may have more variation in the total power. Another possibility is that the CA3 LFP signature for SIA is different from that in CA1, making it necessary to optimize the detection specifically for this brain region. Analysis of intracellular properties of CA3 PCs during SIA and other brain states is an interesting area for future study.

In this study, we show that transitions across brain states are reflected by coordinated changes in subthreshold intracellular dynamics of CA3 PCs. We propose that while theta and LIA induce different changes in cellular and network properties, these are balanced to ensure that only select cells participate in the active neuronal ensemble. During theta, a small subpopulation of CA3 PCs is selectively activated by depolarization while most CA3 PCs are silenced by hyperpolarization, ensuring a high signal-to-noise ratio. In contrast, during LIA, an increase in synaptic input is offset by a decrease in excitability; only the cells that experience a brief depolarization can increase their firing rate. These data demonstrate that within a cell population, intracellular properties adapt to changes in brain state to maintain sparse coding of the network.

Experimental procedures

All experiments were approved by the Ethical Committee #50 and the French Ministry for Education and Research.

Animals

C57Bl6/j male mice were obtained from Charles River and cared for according to the regulations of the University of Bordeaux/CNRS Animal Care and Use Committee. Animals were housed with their littermates with *ad libitum* access to food and water. Cages were kept in a temperature-regulated room on a 12 h light/dark cycle. Electrophysiological recordings were performed on P45-to-P71 mice.

Surgery

Headbar implantation

Custom-made stainless steel head bars (35x3x3 mm) were affixed to the skulls of 4-to-5-week-old mice using Superbond (Phymep) and dental acrylic (Dentalon, Phymep) while under isoflurane anesthesia. The skull underneath the head implant opening was covered with superbond and future locations for the craniotomies above CA3 were marked using stereotactic coordinates (2.0 caudal, 2.0 lateral from bregma).

Craniotomy

The day of recording, animals were anesthetized using isoflurane and a craniotomy (~1.5 mm diameter) was drilled at previously marked location. The dura was left intact and craniotomy was covered with silicone elastomer (Kwik-cast, World Precision Instruments). Mice were placed in a recovery cage for at least 1.5 hours before recording. Mice were typically recorded over two consecutive days.

Training

After headbar implantation, mice were left 2-3 days for recovery, until they started to gain weight again. On the first day of training, mice were allowed to freely explore the wheel for 15 min without being headfixed. During the following 4 days, mice were progressively headfixed (10 min, 30 min, 60 min, and 120 min). Thereafter, mice were headfixed 120 min each day until they habituated and were alternating between running and stopping without showing signs of excessive stress (freezing, escape attempts, struggling, excessive excretion, vocalization). Typically, mice habituated in 2 to 10 days. During the final two days of training, mice were headfixed on the principal wheel used for the recordings and habituated to the ambient light and noises that would occur during a typical experiment.

Recordings

Whole-cell recordings

Before attempting whole-cell patching, the depth of the pyramidal cell layer was detected using an extracellular electrode. Extracellular electrodes were glass patch electrodes (World Precision Instruments) prepared with a vertical puller PC-10 (Narishige) and then broken so that the resistance when filled with standard Ringer's solution (in mM : 135 NaCl, 5.4 KCl, 5 HEPES, 1.8 $CaCl_2$, and 1 $MgCl_2$) was 0.8–1.5 MΩ. The extracellular electrode used to determine the pyramidal cell depth for whole-cell recording was mounted vertically on a micromanipulator (Scientifica). As the electrode was advanced through the cortex, the CA1 pyramidal cell layer was identified when multi unit activity could be detected and the amplitude of ripples increased, typically 1.3–1.5 mm below the surface of the brain. The polarity of the sharp waves inversed below the CA1 pyramidal layer, and the electrode was advanced further down the hippocampus until the sharp waves changed polarity again (to positive) and multi-unit activity was detected, indicative of the CA3 pyramidal layer. The extracellular electrode to be used for LFP recordings during whole-cell patching was mounted on a second micromanipulator (Luigs and Neumann) at a 22.5° angle relative to the vertical axis, and advanced through the same craniotomy at a more medial and caudal position. This

extracellular electrode was advanced until detection of the pyramidal cell layer but not through it. The two LFPs were recorded for visual confirmation of a high correlation between the two signals (phase of theta, coincidence of ripples, multi-unit activity), indicative of a short distance between the two recording sites. Whole-cell patch electrodes (3.5-5 MΩ) were prepared beforehand, and were filled with a solution containing (in mM) 120 K-methanesulfonate, 2 KCl, 10 HEPES, 10 EGTA, 2 MgCl2, and 2 Na-ATP, at 290–300 mOsm and pH 7.2–7.3 adjusted with KOH. The intracellular solution was supplemented with 0.2% (w/v) biocytin for post hoc cellular identification and morphological reconstruction. Whole-cell patch-clamp recordings were achieved using a standard blind-patch approach as previously described (Lee et al., 2009; Margrie et al., 2002). Access resistance and membrane capacitance of the cells were monitored on-line with the membrane test feature of the acquisition software and analyzed off-line. The mean access resistance was 52.4 ± 2.5 MΩ. The membrane potential was not corrected for the liquid junction potential. Recordings were discarded when the access resistance exceeded 100 MΩ or when the action potential peak dropped below 0 mV.

Data acquisition

Electrophysiology

All recordings were made in the current-clamp configuration. Recordings were obtained with a Multiclamp 700B amplifier connected to the Digidata 1440A system. Data were acquired with pClamp 10 (Molecular Devices), digitized at 10 kHz, filtered at 3 kHz, and analyzed off-line with Clampfit 10.4 (Molecular Devices) and Python. To measure input resistance, we injected trains of current pulses (-100 pA, 100 ms) in a separate set of recordings (n = 13).

Pupil recording

Pupil diameter data was measured for a subset of recordings (n=11/35). To measure pupil diameter, the mouse was illuminated with an infrared (850 nm) battery-operated light (Maketheone IR Torch 850NM) and imaged with a camera (DALSA GENIE NANO-M1280-NIR) at 10 Hz.

Locomotion

Online running behavior and the animal's velocity during the recording session was measured using Poly Wheel software (Imetronic, France) and acquired at 32 Hz. Locomotion was detected as IR-sensor-crossing by the animal. 16 sensors were located on a wheel of 20 cm diameter.

Histology

To recover the morphology of neurons filled with biocytin during *in vivo* whole-cell patch-clamp recordings, brains were removed after the completion of electrophysiology experiments and were fixed for 1 week at 4°C in a solution containing 4% PFA in 1X PBS, pH7.4. Coronal slices (100 µm thick) were incubated overnight at 4°C in 1:1000 Alexa Fluor 488 conjugated in the same solution. Images were acquired using a confocal microscope (TCS SP8, Leica) and oil objective HC PL APO 40x/1.30.

Analysis

LFP

LFP signal was downsampled 10 times to 2000 Hz and filtered using a 4-pole butterworth band-pass filter between 0.2 Hz and 100 Hz. After filtering, LFP was again downsampled to 200 Hz. The spectrogram of the LFP was calculated using consecutive fast Fourier transforms within ~2 second boxcar windows with 90% overlap. Theta (6-9 Hz), delta (0.5-3.5 Hz) and gamma (30-50 Hz) powers were extracted from the spectrogram. Then theta/delta powers and LFP power between 0.5 Hz and 80 Hz were z-scored.

Brain state classification

Start of theta events were classified as positive theta/delta powers. To be counted as theta events, theta bouts had to be longer than 1 s and have a power higher than 1 sd above the mean at least once. If too theta bouts happened less than 1 s apart, they were merged into one single theta period. Start of LIA events were classified as LFP power above the mean (between 0.5 Hz and 80 Hz). To be counted as LIA events, LIA bouts had to be longer than 2 s and have a power higher than 0.25 sd above the mean at least once. If two LIA bouts happened less than 0.5 s apart, they were merged into one single LIA period.

Membrane potential

Analysis of Vm changes was performed on Vm traces after spike removal. Spikes were detected when the derivative of the Vm (dV/dt) exceeded 5 mV/ms. To keep a conservative estimate of average Vm, spikes and their underlying depolarizations such as plateau potentials were removed (Figure S1A). The spike-removed Vm trace was then smoothed by taking the mean over a sliding window of 2 s, and the smoothed Vm was downsampled to 20 Hz. The residual Vm trace was obtained by subtracting the smoothed Vm from the spike-removed Vm. From this residual Vm, the variance was calculated over a sliding a window of 1 s. The variance trace was then smoothed by taking the mean over a sliding window of 2 s and downsampled to 20 Hz.

Distance to spike threshold

The time stamp and threshold potential for each spike was taken as the time and Vm when the first derivative (dV/dt) first surpassed 10 V/s. To restrict the analysis to spikes that were either isolated or the first in a burst, spikes that has a prior inter-spike interval of less than 50 ms were eliminated from the analysis. Spikelets were also eliminated by discarding spikes that did not reach peak amplitude of at least -10 mV and a peak dV/dt of at least 50 V/s. The distance to spike threshold for each spike was calculated by subtracting the spike threshold from the mean Vm over a specified period prior to the spike; this mean value was calculated from the 20 kHz Vm trace after spike removal.

Pupil diameter

To measure pupil diameter, frames were extracted from the video file. A Circle Hough Transform (CHT) was performed to detect circular objects in each individual frames. The Radius of the detected circles was extracted automatically. Pupil diameter data was included after control of correct pupil detection. The resulting pupil diameter trace was smoothed with a 4-pole butterworth low-pass filter (0.5 Hz cutoff).

Statistics

Unless otherwise noted, data were expressed as the median +/- the mean absolute derivation about the median, which was calculated by subtracting each data point from the group's median, taking the absolute value, summating, and then dividing by the number of data points. These measures of central tendency and variation were used because many distributions were found not to be normal. When comparing 2 groups, a bootstrapping method was used. Briefly, data from both groups were randomly resampled with replacement to form two surrogate groups. This was repeated 1,000 times, and if the difference in medians was more extreme than 95% of the surrogate trials, the groups were considered significantly different. For comparisons of 3 or more groups, a Kruskal-Wallis test was performed to determine the presence of any significantly different group before performing the 2-group bootstrap for each group pair. A different bootstrap test was used when comparing two non-independent groups. In this test, the difference between paired data points was randomly determined to be either positive or negative 1,000 times. If the mean of the differences in the actual data set was more extreme than 95% of those in the shuffled data set, the paired groups were considered to have a significant difference. For comparative scatter plots where variables during different states were compared, a Mann-Whitney U test was used to determine whether there was a significant difference between the states for that particular cell (filled circles in scatter plots). When determining whether a value was significantly different from zero, a bootstrapping method was used. The distribution was demeaned and then resampled with replacement

10,000 times. If the mean of the original data was more extreme than 95% of the resampled means, it was considered significantly different from zero.

To determine whether a particular event was associated with a significant change in Vm, 2 two-second windows of the 20 Hz downsampled Vm around the start of the event were compared with a Welch's t-test. For theta, the comparison was made between –2.5 to –0.5 and 0.5 to 2.5 seconds with respect to the start of the event; for LIA, the windows were –4 to –2 and –1 to 1 second. Events with p-values less than 0.05 were considered to be hyper- or depolarizing depending on the direction of the change in Vm. To determine whether the proportions of hyperpolarizing, depolarizing and no change events could be due to chance, a bootstrapping method was used. For every recording, the actual event times were replaced with randomly-sampled times, and the same method as previously described was used to determine whether each random timepoint was associated with a hyperpolarization, depolarization, or no change. This was repeated 1,000 times to create a distribution of proportions. Proportions were considered significantly different from chance if they were either greater or smaller than 95% of the randomly-sampled data sets.

To determine whether a cell was consistently changed Vm at the start of a particular type of event, we used a bootstrapping method. Over a single recording session, the Vm and actual event times were shifted in time with respect to one another 6,000 times in increments of 50 ms. For each shift, the average change in Vm associated with event onset was calculated for the cell. Cells were considered significantly hyper- or depolarizing when the average change in Vm was more extreme than 95% of the shuffled data.

Ackowledgements

This study was supported by the Centre National de la Recherche Scientifique, the European Commission (EIF Fellowship awarded to AK), the ANR (grant Hippencode), and the Fondation pour la Recherche Médicale (to MM). We are grateful to Ania Gonçalves for help in confocal imaging and Mario Carta for fruitful discussions.

References

Adam, Y., Kim, J.J., Lou, S., Zhao, Y., Xie, M.E., Brinks, D., Wu, H., Mostajo-Radji, M.A., Kheifets, S., Parot, V., et al. (2019). Voltage imaging and optogenetics reveal behaviour-dependent changes in hippocampal dynamics. Nature.

Azouz, R., and Gray, C.M. (2003). Adaptive coincidence detection and dynamic gain control in visual cortical neurons in vivo. Neuron *37*, 513–523.

Berry, S.D., and Thompson, R.F. (1978). Prediction of learning rate from the hippocampal electroencephalogram. Science *200*, 1298–1300.

Bittner, K.C., Grienberger, C., Vaidya, S.P., Milstein, A.D., Macklin, J.J., Suh, J., Tonegawa, S., and Magee, J.C. (2015). Conjunctive input processing drives feature selectivity in hippocampal CA1 neurons. Nat. Neurosci. *18*, 1133–1142.

Buzsáki, G. (1986). Hippocampal sharp waves: their origin and significance. Brain Res. *398*, 242–252.

Buzsáki, G. (2015). Hippocampal sharp wave-ripple: A cognitive biomarker for episodic memory and planning. Hippocampus *25*, 1073–1188.

Buzsáki, G., and Moser, E.I. (2013). Memory, navigation and theta rhythm in the hippocampal-entorhinal system. Nat. Neurosci. *16*, 130–138.

Carr, M.F., Jadhav, S.P., and Frank, L.M. (2011). Hippocampal replay in the awake state: A potential substrate for memory consolidation and retrieval. Nat. Neurosci. *14*, 147–153.

Cohen, M.X. (2017). Where Does EEG Come From and What Does It Mean? Trends Neurosci. *40*, 208–218.

Crochet, S., and Petersen, C.C.H. (2006). Correlating whisker behavior with membrane potential in barrel cortex of awake mice. Nat. Neurosci. *9*, 608–610.

Eichenbaum, H. (2016). Still searching for the engram. Learn. Behav. *44*, 209–222.

Ekstrom, A.D., Caplan, J.B., Ho, E., Shattuck, K., Fried, I., and Kahana, M.J. (2005). Human hippocampal theta activity during virtual navigation. Hippocampus *15*, 881–889.

English, D.F., Peyrache, A., Stark, E., Roux, L., Vallentin, D., Long, M.A., Buzsaki, G., and Buzsáki, G. (2014). Excitation and Inhibition Compete to Control Spiking during Hippocampal Ripples: Intracellular Study in Behaving Mice. J Neurosci *34*, 16509–16517.

Epsztein, J., Brecht, M., and Lee, A.K. (2011). Intracellular Determinants of Hippocampal CA1 Place and Silent Cell Activity in a Novel Environment. Neuron *70*, 109–120.

Foster, D.J., and Wilson, M.A. (2006). Reverse replay of behavioural sequences in hippocampal place cells during the awake state. Nature *440*, 680–683.

Fuhrmann, F., Justus, D., Sosulina, L., Kaneko, H., Beutel, T., Friedrichs, D., Schoch, S., Schwarz, M.K., Fuhrmann, M., and Remy, S. (2015). Locomotion, Theta Oscillations, and the Speed-Correlated Firing of Hippocampal Neurons Are Controlled by a Medial Septal Glutamatergic Circuit. Neuron *86*, 1253–1264.

Gan, J., Weng, S., Pernía-Andrade, A.J., Csicsvari, J., and Jonas, P. (2017). Phase-Locked Inhibition, but Not Excitation, Underlies Hippocampal Ripple Oscillations in Awake Mice In Vivo. Neuron *93*, 1–7.

Green, J.D., and Arduini, A.A. (1954). Hippocampal electrical activity in arousal. J. Neurophysiol. *17*, 533–557.

Grienberger, C., Chen, X., and Konnerth, a (2014). NMDA Receptor-Dependent Multidendrite Ca Spikes Required for Hippocampal Burst Firing In Vivo. Neuron *81*, 1274–1281.

Gupta, A.S., Van Der Meer, M.A.A., Touretzky, D.S., and Redish, A.D. (2012). Segmentation of spatial experience by hippocampal theta sequences. Nat. Neurosci. *15*, 1032–1039.

Harvey, C.D., Collman, F., Dombeck, D.A., and Tank, D.W. (2009). Intracellular dynamics of hippocampal place cells during virtual navigation. Nature *461*, 941–946.

Hulse, B.K., Moreaux, L.C., Lubenov, E. V, Siapas Correspondence, A.G., and Siapas, A.G. (2016). Membrane Potential Dynamics of CA1 Pyramidal Neurons during Hippocampal Ripples in Awake Mice. Neuron *89*, 800–813.

Hulse, B.K., Lubenov, E. V., and Siapas, A.G. (2017). Brain State Dependence of Hippocampal Subthreshold Activity in Awake Mice. Cell Rep. *18*, 136–147.

Jarosiewicz, B., and Skaggs, W.E. (2004). Level of Arousal During the Small Irregular Activity State in the Rat Hippocampal EEG. J. Neurophysiol. *91*, 2649–2657.

Jarosiewicz, B., McNaughton, B.L., and Skaggs, W.E. (2002). Hippocampal population activity during the small-amplitude irregular activity state in the rat. J. Neurosci. *22*, 1373–1384.

Jutras, M.J., Fries, P., and Buffalo, E.A. (2013). Oscillatory activity in the monkey hippocampus during visual exploration and memory formation. Proc. Natl. Acad. Sci. U. S. A. *110*, 13144–13149.

Kay, K., Sosa, M., Chung, J.E., Karlsson, M.P., Larkin, M.C., and Frank, L.M. (2016). A hippocampal network for spatial coding during immobility and sleep. Nature *531*, 185–190.

Kesner, R.P., and Rolls, E.T. (2015). A computational theory of hippocampal function, and tests of the theory: New developments. Neurosci. Biobehav. Rev. *48*, 92–147.

Komisaruk, B.R. (1970). Synchrony between limbic system theta activity and rhythmical behavior in rats. J. Comp. Physiol. Psychol. *70*, 482–492.

Kowalski, J., Gan, J., Jonas, P., and Pernía-Andrade, A.J. (2016). Intrinsic membrane properties determine hippocampal differential firing pattern in vivo in anesthetized rats. Hippocampus *26*, 668–682.

Landfield, P.W., Mcgaugh, J.L., and Tusa, R.J. (1972). Theta rhythm: A temporal correlate of memory storage processes in the rat. Science (80-.). *175*, 87–89.

Lee, A.K., and Wilson, M.A. (2002). Memory of sequential experience in the hippocampus during slow wave sleep. Neuron *36*, 1183–1194.

Lee, A.K., Epsztein, J., and Brecht, M. (2009). Head-anchored whole-cell recordings in freely moving rats. Nat. Protoc. *4*, 385–392.

Leutgeb, J.K., Leutgeb, S., Moser, M.-B., and Moser, E.I. (2007). Pattern separation in the dentate gyrus and CA3 of the hippocampus. Science *315*, 961–966.

Macrides, F., Eichenbaum, H.B., and Forbes, W.B. (1982). Temporal relationship between sniffing and the limbic theta rhythm during odor discrimination reversal learning. J. Neurosci. *2*, 1705–1717.

Maier, N., Tejero-Cantero, Á., Dorrn, A.L., Winterer, J., Beed, P.S., Morris, G., Kempter, R., Poulet, J.F.A.,

Leibold, C., and Schmitz, D. (2011). Coherent Phasic Excitation during Hippocampal Ripples. Neuron *72*, 137–152.

Marder, E., O'Leary, T., and Shruti, S. (2014). Neuromodulation of Circuits with Variable Parameters: Single Neurons and Small Circuits Reveal Principles of State-Dependent and Robust Neuromodulation. Annu. Rev. Neurosci. *37*, 329–346.

Margrie, T.W., Brecht, M., and Sakmann, B. (2002). In vivo, low-resistance, whole-cell recordings from neurons in the anaesthetized and awake mammalian brain. Pflugers Arch. Eur. J. Physiol. *444*, 491–498.

Marr, D. (1971). Simple Memory: A Theory for Archicortex. Philos. Trans. R. Soc. B Biol. Sci. *262*, 23–81.

McGinley, M.J., Vinck, M., Reimer, J., Batista-Brito, R., Zagha, E., Cadwell, C.R., Tolias, A.S., Cardin, J.A., and McCormick, D.A. (2015). Waking State: Rapid Variations Modulate Neural and Behavioral Responses. Neuron *87*, 1143–1161.

Mizuseki, K., Sirota, A., Pastalkova, E., and Buzsáki, G. (2009). Theta Oscillations Provide Temporal Windows for Local Circuit Computation in the Entorhinal-Hippocampal Loop. Neuron *64*, 267–280.

Nakazawa, K., Sun, L.D., Quirk, M.C., Rondi-Reig, L., Wilson, M.A., and Tonegawa, S. (2003). Hippocampal CA3 NMDA receptors are crucial for memory acquisition of one-time experience. Neuron *38*, 305–315.

O'Keefe, J. (1976). Place units in the hippocampus of the freely moving rat. Exp. Neurol. *51*, 78–109.

Polack, P.O., Friedman, J., and Golshani, P. (2013). Cellular mechanisms of brain state-dependent gain modulation in visual cortex. Nat. Neurosci. *16*, 1331–1339.

Poulet, J.F. a, and Petersen, C.C.H. (2008). Internal brain state regulates membrane potential synchrony in barrel cortex of behaving mice. Nature *454*, 881–885.

Ramirez-Villegas, J.F., Logothetis, N.K., and Besserve, M. (2015). Diversity of sharp-wave–ripple LFP signatures reveals differentiated brain-wide dynamical events. Proc. Natl. Acad. Sci. *112*, E6379–E6387.

Rebola, N., Carta, M., and Mulle, C. (2017). Operation and plasticity of hippocampal CA3 circuits: Implications for memory encoding. Nat. Rev. Neurosci. *18*, 209–221.

Schneider, D.M., Nelson, A., and Mooney, R. (2014). A synaptic and circuit basis for corollary discharge in the auditory cortex. Nature *513*, 189–194.

Spruston, N., Jaffe, D.B., Williams, S.H., and Johnston, D. (1993). Voltage- and space-clamp errors associated with the measurement of electrotonically remote synaptic events. J. Neurophysiol. *70*, 781–802.

Taxidis, J., Anastassiou, C.A., Diba, K., and Koch, C. (2015). Local Field Potentials Encode Place Cell Ensemble Activation during Hippocampal Sharp Wave Ripples. Neuron *87*, 590–604.

Vanderwolf, C.H. (1969). Hippocampal electrical activity and voluntary movement in the rat. Electroencephalogr. Clin. Neurophysiol. *26*, 407–418.

Whishaw, I.Q., and Vanderwolf, C.H. (1971). Hippocampal EEG and behavior: effects of variation in body temperature and relation of EEG to vibrissae movement, swimming and shivering. Physiol. Behav. *6*, 391–397.

Wixted, J.T., Squire, L.R., Jang, Y., Papesh, M.H., Goldinger, S.D., Kuhn, J.R., Smith, K.A., Treiman, D.M., and Steinmetz, P.N. (2014). Sparse and distributed coding of episodic memory in neurons of the human hippocampus. Proc. Natl. Acad. Sci. *111*, 9621–9626.

Zucca, S., Griguoli, M., Malézieux, M., Grosjean, N., Carta, M., and Mulle, C. (2017). Control of Spike Transfer at Hippocampal Mossy Fiber Synapses In Vivo by GABA A and GABA B Receptor-Mediated Inhibition. J. Neurosci. *37*, 587–598.

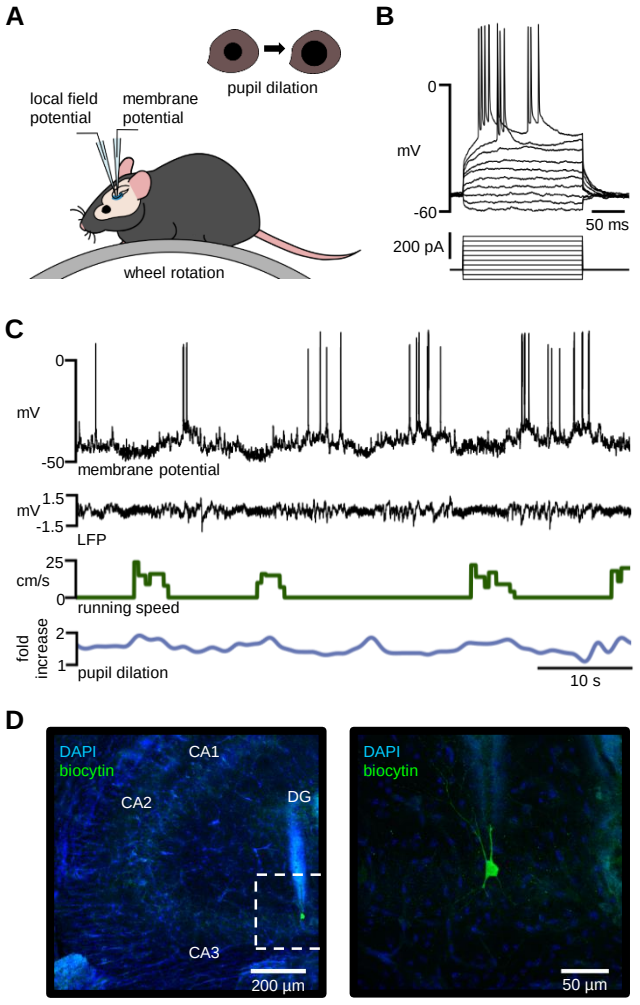
A
pupil dilation
local field potential
membrane potential
wheel rotation
B
0
mV
-60
50 ms
200 pA
C
0
mV
-50
membrane potential
1.5
mV
-1.5
LFP
25
cm/s
0
running speed
2
fold increase
1
pupil dilation
10 s
D
DAPI
biocytin
CA1
CA2
DG
CA3
200 µm
DAPI
biocytin
50 µm

Figure 1 - Experimental configuration and data recorded. (A) Schematic of the head-fixed electrophysiological recording configuration. LFP and whole-cell recordings were performed in CA3. Wheel rotation and pupil dilation of the animal were monitored during the recordings. (B) Example trace of the sub- and suprathreshold responses of a CA3 PC to injected current pulses (10 pulses, from -80 pA to 280 pA). (C) Example trace of a simultaneous current-clamp recording from a CA3 PC showing spontaneous action potentials (membrane potential, black), aligned with the nearby LFP (LFP, black) the corresponding locomotor velocity (running speed, green) and pupil diameter changes (pupil dilation, blue) of the animal. (D) Confocal fluorescent image of a 100-µm-thick coronal section of dorsal hippocampus (left; 20x) with a single CA3 PC (right; 40x) filled with biocytin during whole-cell recording and visualized by post hoc labeling with Alexa Fluor 488. Note the presence of the pipette track above the filled CA3 PC.

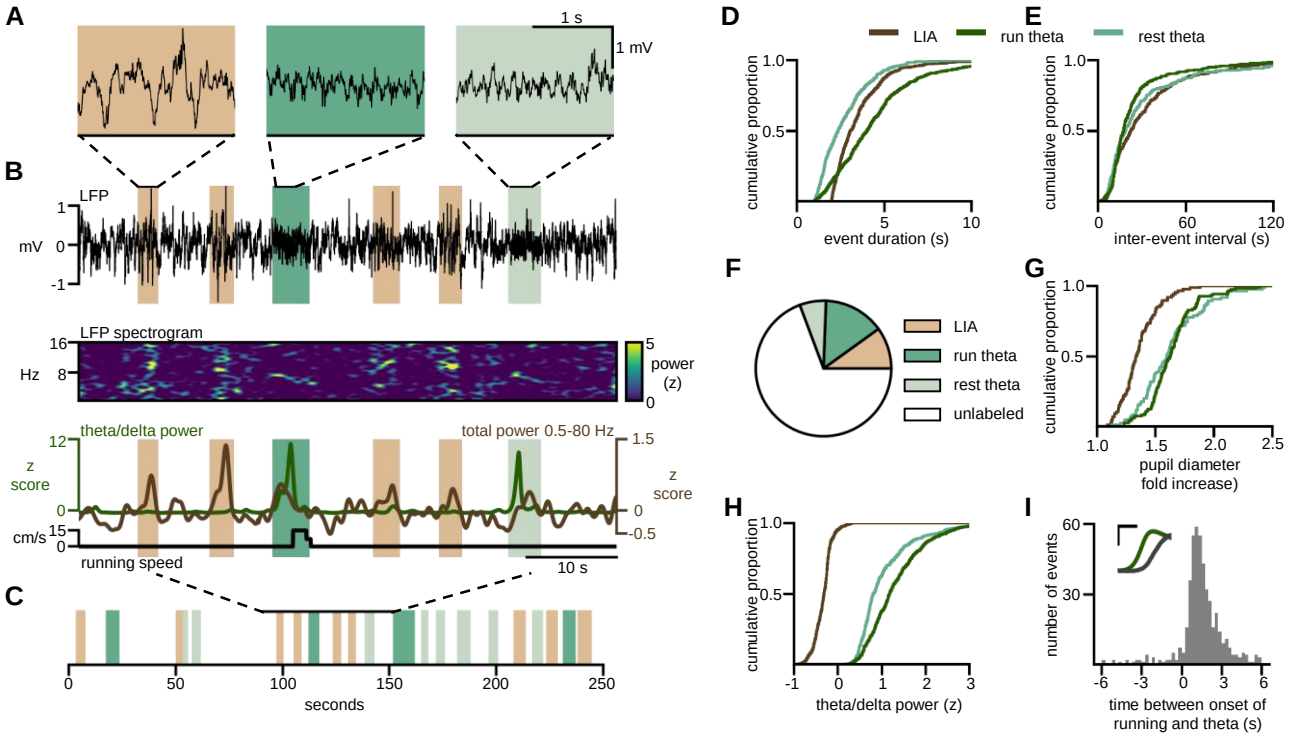
A
1 s
1 mV
B
LFP
1
mV 0
-1
LFP spectrogram
16
Hz 8
5
power
(z)
0
theta/delta power
total power 0.5-80 Hz
12
z
score
0
1.5
z
score
0
-0.5
cm/s 15
0
running speed
10 s
C
0
50
100
150
200
250
seconds
D
LIA
run theta
rest theta
cumulative proportion
1.0
0.5
0
5
10
event duration (s)
E
cumulative proportion
1.0
0.5
0
60
120
inter-event interval (s)
F
LIA
run theta
rest theta
unlabeled
G
cumulative proportion
1.0
0.5
1.0
1.5
2.0
2.5
pupil diameter
fold increase)
H
cumulative proportion
1.0
0.5
-1
0
1
2
3
theta/delta power (z)
I
number of events
60
30
-6
-3
0
3
6
time between onset of
running and theta (s)

Figure 2 - Brain state classification and characterization. (A) Example traces of LIA (brown), run theta (dark green) and rest theta (light green). Similar color scheme is used throughout. (B) Top: One minute LFP recording from CA3 with detected LIA, run theta and rest theta. Middle: Corresponding spectrogram showing z-scored LFP power between 0 and 16 Hz. Note the high broadband power present during LIA and narrow frequency band during theta events. Bottom: Theta/delta power ratio superimposed with total 0.5-80 Hz power, used in state detection. Velocity of the animal is shown below. (C) Representation of the brain states LIA, run theta and rest theta over a full recording session. (D) (E) Cumulative distribution of the duration (D) and inter-event interval (E) of the different states. Run theta events lasted longer than rest theta and LIA events (4.02 ± 1.89 s [n = 519 events] for run theta, 2.37 ± 1.11 s [n = 371 events] for rest theta, 3.07 ± 1.11 s [n = 450 events] for LIA, $p < 0.001$ for both pairs). LIA events lasted longer than rest theta ($p < 0.001$). All data are expressed in median ± average absolute deviation from the median unless otherwise stated. Run and rest theta occurred at a similar frequency ($p = 0.158$). Both types of theta occurred more often than LIA (17.73 ± 18.03 s [n = 519 events] for run theta, 19.14 ± 23.75 s [n = 371 events] for rest theta, 23.12 ± 21.93 s [n = 450 events] for LIA, run theta vs LIA $p < 0.001$, rest theta vs LIA $p = 0.023$). (F) Total percent of time detected for each state over all the recording sessions. Over 269.6 minutes of recording there were a total of 39.1 minutes of run theta (14.5%), 17.0 minutes of rest theta (6.3%), and 26.7 minutes of LIA (9.9%). The remaining 186.9 minutes (69.3%) were left unlabeled. (G) Pupil diameter (expressed as fold increase from the minimum) during each brain state (n = 12 cells). The pupil dilated the same amount for run and rest theta ($p=0.354$), but was more dilated during both types of theta events than during LIA (1.63 ± 0.15 fold [n = 122 events] for run theta, 1.6 ± 0.21 fold [n = 85 events] for rest theta, 1.34 ± 0.12 fold [n = 87 events] for LIA, $p < 0.001$ for both pairs). (H) Theta/delta power ratio for each brain state. The z-scored theta/delta power was larger during theta than during LIA (1.19 ± 0.51 [n = 519 events] for run theta, 0.82 ± 0.46 [n = 371 events] for rest theta, -0.31 ± 0.15 [n = 450 events] for LIA, $p < 0.001$ for both pairs). This ratio was also larger during run theta compared to rest theta ($p < 0.001$). (I) Delay between the start of theta and start of running. Inset shows the average increase in theta preceding the average increase in velocity (grey) for all events (n = 517) in all cells recorded (scale bar represents 1 s, 1 unit of z-scored theta/delta ratio, 5 cm/s). Running started significantly after the start of theta (1.3 ± 5.02 s, $p < 0.001$).

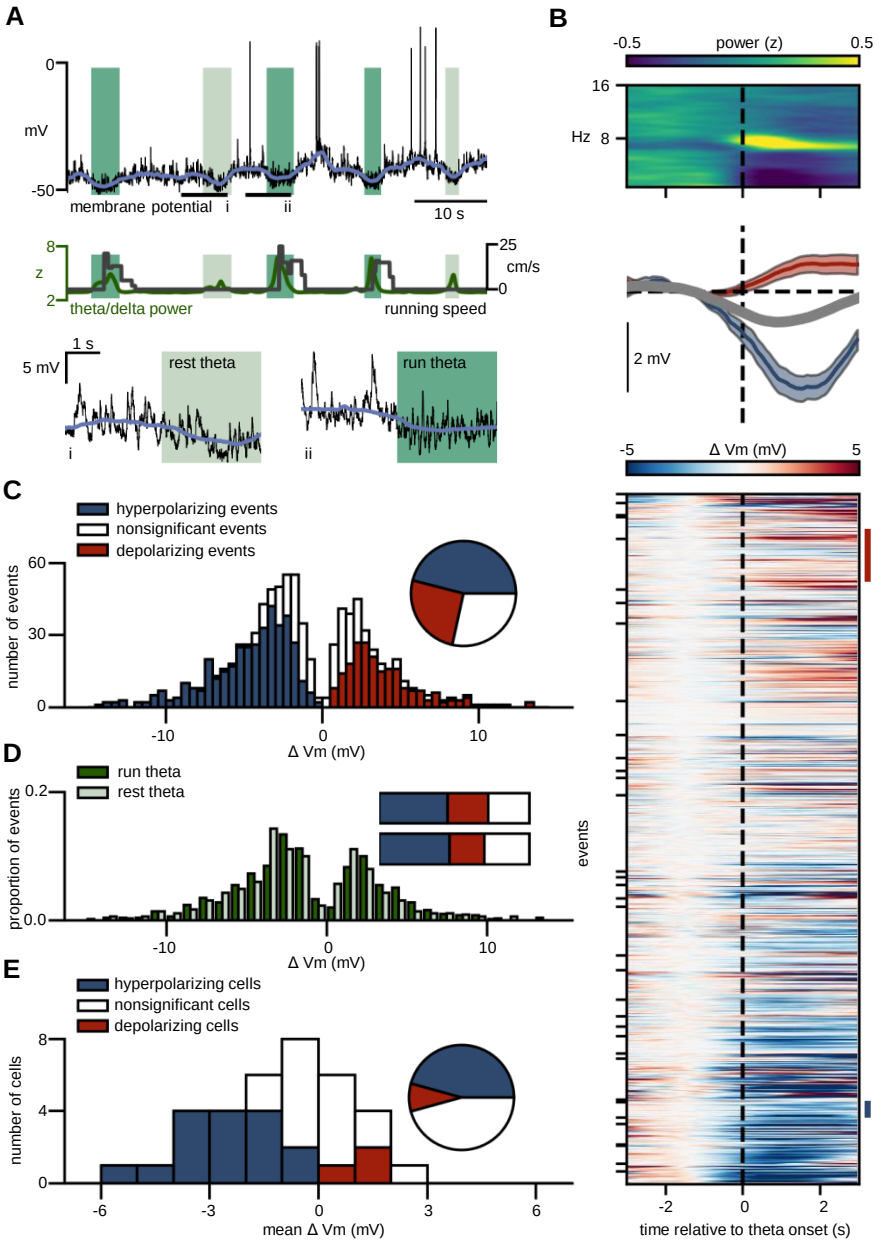
A
0
mV
-50
membrane potential
i
ii
10 s
8
z
2
theta/delta power
25
cm/s
0
running speed
1 s
5 mV
rest theta
run theta
i
ii
B
-0.5
power (z)
0.5
16
Hz
8
2 mV
-5
Δ Vm (mV)
5
events
-2
0
2
time relative to theta onset (s)
C
hyperpolarizing events
nonsignificant events
depolarizing events
60
30
0
number of events
-10
0
10
Δ Vm (mV)
D
run theta
rest theta
0.2
0.0
proportion of events
-10
0
10
Δ Vm (mV)
E
hyperpolarizing cells
nonsignificant cells
depolarizing cells
8
4
0
number of cells
-6
-3
0
3
6
mean Δ Vm (mV)

Figure 3 - CA3 pyramidal cells decrease their membrane potential and firing rate during theta. (A) Example trace showing a whole-cell recording of a CA3 PC (top), with simultaneous theta/delta power ratio of the nearby LFP and the running speed of the mouse (middle). Blue trace superimposed on the raw Vm is the smoothed Vm after spike removal. Bottom: examples of Vm modulation during one rest theta and one run theta event. (B) Top: Spectrogram of the average LFP (z-scored within frequency bands) triggered by transitions to theta (time = 0, dotted line) showing an increase of power in the theta band (6-9 Hz). Middle: Average Vm traces during theta onset of an example hyperpolarizing (blue) and depolarizing (red) cell, as well as the grand average over all events (grey) (n = 848, shaded areas represent ± sem). Bottom: Color plot showing the Vm of CA3 PCs triggered by transition to theta normalized to 2.5 to 0.5 s before start of theta. Blue represents Vm hyperpolarization, red Vm depolarization. Each cell is represented in between black ticks. Cells are ordered depending on their average Vm modulation during theta, with depolarizing cells on top and hyperpolarizing cells at the bottom of the plot. Events within each cell are ordered by the time in which they occurred in the recording. Red and blue vertical lines indicate the sample cells shown in the average traces above. (C) Distribution of the magnitude of change in Vm at the onset of theta (n = 848 events, bin size = 0.5 mV). Events are colored according to whether there was a hyperpolarization (blue), depolarization (red) or no significant change (white). Similar color scheme is used throughout the figures. Inset: pie chart of the different event types (46.0% hyperpolarizing [n = 390 events], 25.6% depolarizing [n = 217 events], 28.4% no change [n = 241 events]. Compared to a shuffled data set, there were significantly more hyperpolarizing events and less depolarizing and nonsignificant events ($p < 0.001$ for all categories) than chance level. (D) Comparison of Vm modulation during theta for run [n = 495] and rest [n = 353] events (bin size = 1 mV). Inset: bar charts of percent event type (hyperpolarizing, depolarizing, or no change) for run (top) and rest (bottom) theta events. All types of events occurred at a similar frequency during run and rest theta ($p=0.417$ for hyperpolarizing, $p=0.802$ for depolarizing, $p=0.219$ for no change). (E) Distribution of cells' average Vm change during theta (bin size = 1 mV). Inset: pie chart of the different cell types (16 cells were hyperpolarizing, 3 cells were depolarizing and 16 cells showed no significant modulation towards one specific direction).

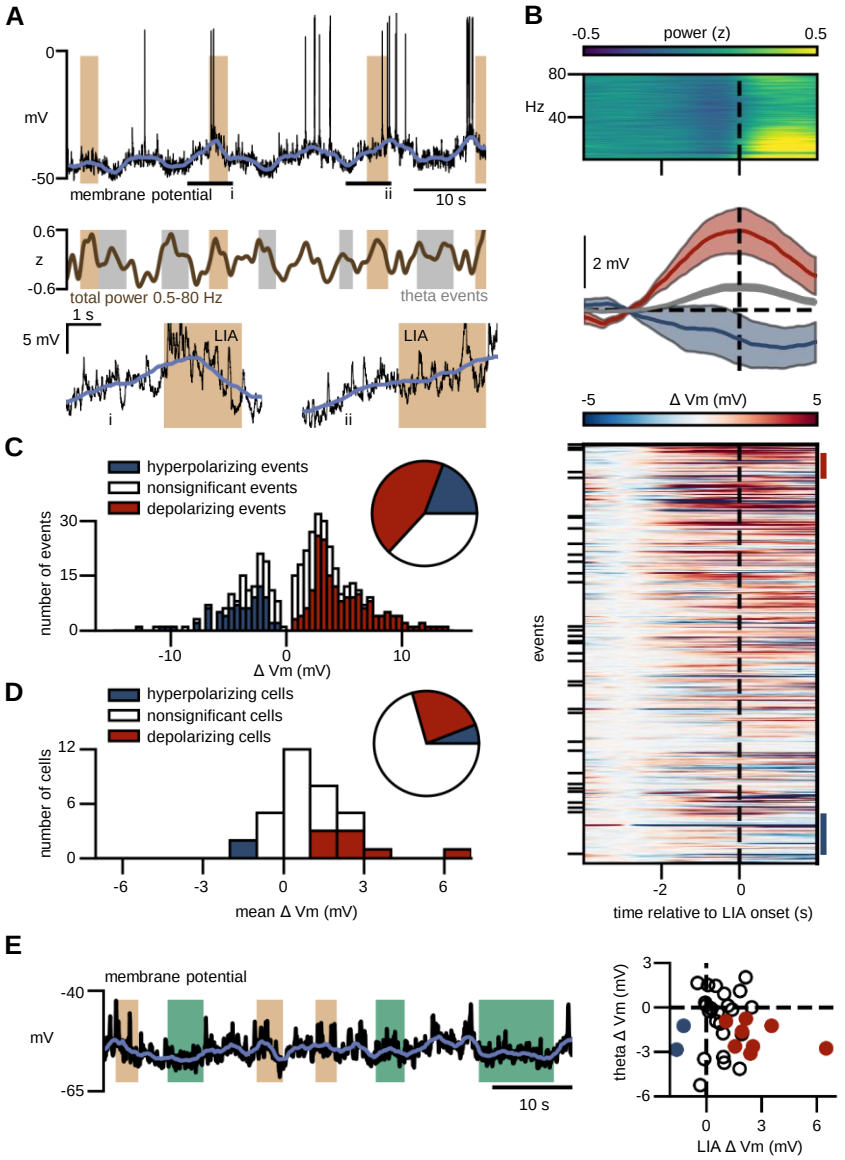
A
0
mV
-50
membrane potential
i
ii
10 s
0.6
z
-0.6
total power 0.5-80 Hz
theta events
1 s
5 mV
LIA
LIA
i
ii
B
-0.5
power (z)
0.5
80
Hz
40
2 mV
-5
Δ Vm (mV)
5
events
-2
0
time relative to LIA onset (s)
C
hyperpolarizing events
nonsignificant events
depolarizing events
number of events
30
15
0
-10
0
10
Δ Vm (mV)
D
hyperpolarizing cells
nonsignificant cells
depolarizing cells
number of cells
12
6
0
-6
-3
0
3
6
mean Δ Vm (mV)
E
membrane potential
-40
mV
-65
10 s
theta Δ Vm (mV)
3
0
-3
-6
0
3
6
LIA Δ Vm (mV)

Figure 4 - CA3 pyramidal cells increase their membrane potential during LIA. (A) Example trace showing a whole-cell recording of a CA3 PC (top) with simultaneous total power (0.5-80 Hz) of the nearby LFP (middle). Previously detected theta events are shown in grey since they were excluded from being classified as LIA states. Blue trace superimposed on the raw Vm is the smoothed Vm after spike removal. Bottom: two examples of Vm modulation during LIA events. (B) Spectrogram of the average LFP (z-scored within frequency bands) triggered by transitions to LIA (time = 0, dotted line) showing an increase in broadband power after the start of LIA. Middle: Average Vm traces during theta onset of an example hyperpolarizing (blue) and depolarizing (red) cell, as well as the grand average over all events (grey) (n = 426, shaded areas represent ± sem). Bottom: Color plot showing the Vm of CA3 PCs triggered by transition to LIA normalized to 4 to 2 s before start of LIA. Blue represents Vm hyperpolarization, red Vm depolarization. Each cell is represented in between black ticks. Cells are ordered depending on their Vm modulation during LIA, with depolarizing cells on top and hyperpolarizing cells at the bottom of the plot. Events within each cell are ordered by the time in which they occurred in the recording. Red and blue vertical lines indicate the sample cells shown in the average traces above. (C) Distribution of the magnitude of change in Vm at the onset of LIA (n = 426 events, bin size = 0.5 mV). Inset: pie chart of the different event types (19.2% hyperpolarizing [n = 82 events], 43.9% depolarizing [n = 187 events], 36.9% no change [n = 157 events]). Compared to a shuffled data set, there were significantly less hyperpolarizing events ($p < 0.001$) and more depolarizing events ($p < 0.001$) than expected by chance. (D) Distribution of cells' average Vm change during LIA (bin size = 1 mV). Inset: pie chart of the different cell types (2 cells were hyperpolarizing, 8 cells were depolarizing and 24 cells showed no significant modulation towards one specific direction). (E) Comparison of direction of Vm modulation during theta versus LIA events. Left: example trace showing a whole-cell recording of a CA3 PC during LIA and theta. Right: Average change in Vm during theta versus average change in Vm during LIA. Filled circles represent significant modulation during LIA, and color represents direction of modulation.

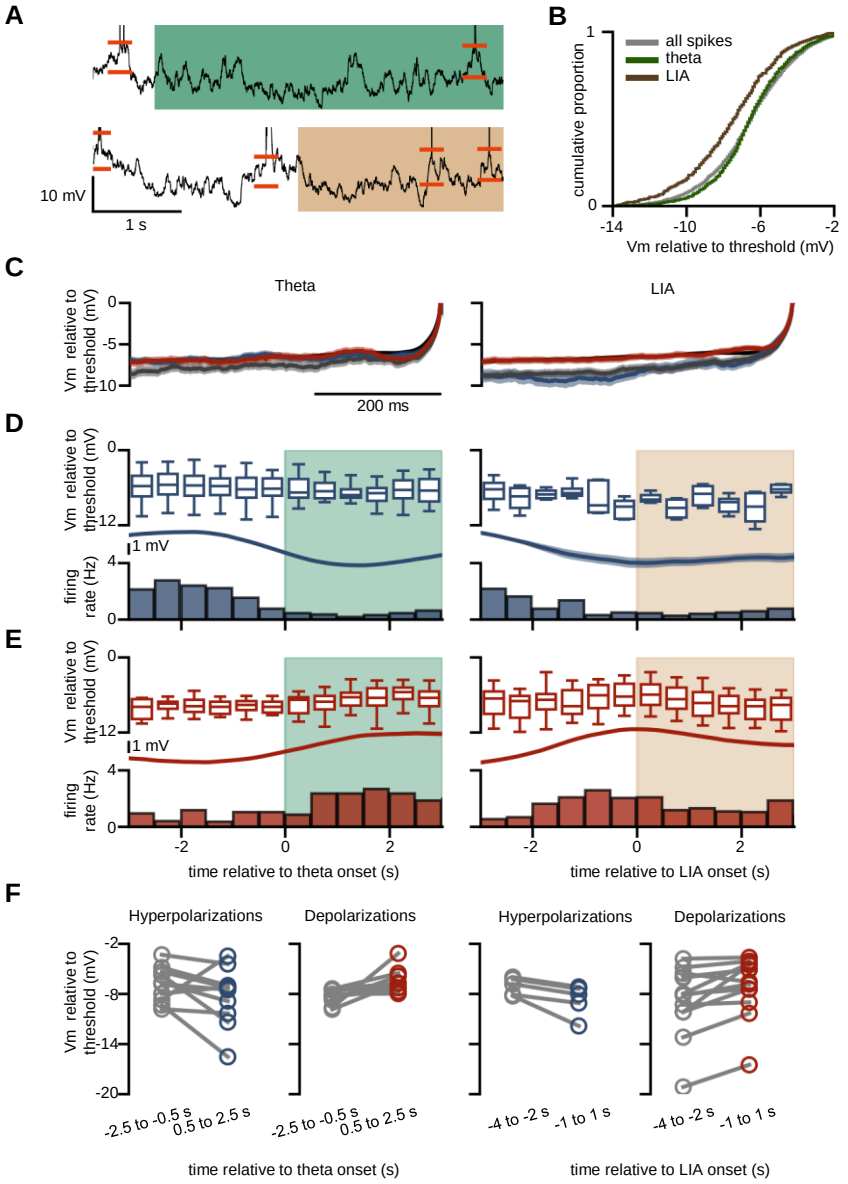
A
10 mV
1 s
B
all spikes
theta
LIA
cumulative proportion
1
0
-14
-10
-6
-2
Vm relative to threshold (mV)
C
Theta
LIA
Vm relative to threshold (mV)
0
-5
-10
200 ms
D
Vm relative to threshold (mV)
0
-12
1 mV
firing rate (Hz)
4
0
E
Vm relative to threshold (mV)
0
-12
1 mV
firing rate (Hz)
4
0
-2
0
2
time relative to theta onset (s)
time relative to LIA onset (s)
F
Hyperpolarizations
Depolarizations
Hyperpolarizations
Depolarizations
Vm relative to threshold (mV)
-2
-8
-14
-20
-2.5 to -0.5 s
0.5 to 2.5 s
-4 to -2 s
-1 to 1 s
time relative to theta onset (s)
time relative to LIA onset (s)

Figure 5 – State-dependent changes in spike threshold relative to membrane potential. (A) Example traces showing, for each spike, the threshold potential (top orange lines) and the average membrane potential during the 500-50 ms prior to the spike (bottom orange lines). Shaded areas indicate an example theta event (green, top), and LIA event (brown, bottom). (B) Cumulative distribution of Vm relative to firing threshold for all spikes occurring during theta (green) and LIA (brown). Those for all recorded spikes are shown in grey for comparison. Vm relative to threshold is lower for spikes occurring during LIA, but there is no difference between those during theta and all spikes (-6.52 ± 1.72 mV [n = 1025 spikes] for theta, -7.42 ± 2.08 mV [n = 566 spikes] for LIA, -6.46 ± 1.92 mV [n = 6750 spikes] for all spikes, $p < 0.001$ for LIA vs all, $p = 0.573$ for theta vs all). Note that for all analyses involving spike threshold, cell #20 was omitted due to an unusually low spike threshold and high firing rate. (C) Average traces of the Vm relative to firing threshold of the 500 ms preceding spike onset for spikes occurring during theta (left), and LIA (right). Spikes comprising each average trace were limited to those occurring within 0.5-2.5 s after event onset for theta, and between 1 s before and 1 s after event onset for LIA. Spikes were further divided depending on whether the event was associated with a significant hyperpolarization (blue), depolarization (red), or no significant change in Vm (grey). The back trace is the average of all spikes and is repeated in both panels for comparison. Shading shows ± SEM. (D) Change in firing properties for events associated with significant hyperpolarizations. Event-triggered changes in firing rate (bottom), Vm (middle), and Vm relative to firing threshold (top) for theta (left) and LIA (right). (E) Same as (D), but for events associated with significant depolarizations. (F) Cells displayed a local change in the Vm relative to spike threshold around the onsets of theta and LIA (-1.44 ± 2.14 mV [n = 10 cells], $p = 0.09$ for theta hyperpolarizations, 1.88 ± 1.43 mV [n = 9 cells], $p = 0.001$ for theta depolarizations [one outlier omitted], -1.64 ± 1.92 mV [n = 5 cells], $p < 0.001$ for LIA hyperpolarizations, 1.65 ± 1.79 mV [n = 13 cells], $p = 0.001$ for LIA depolarizations).

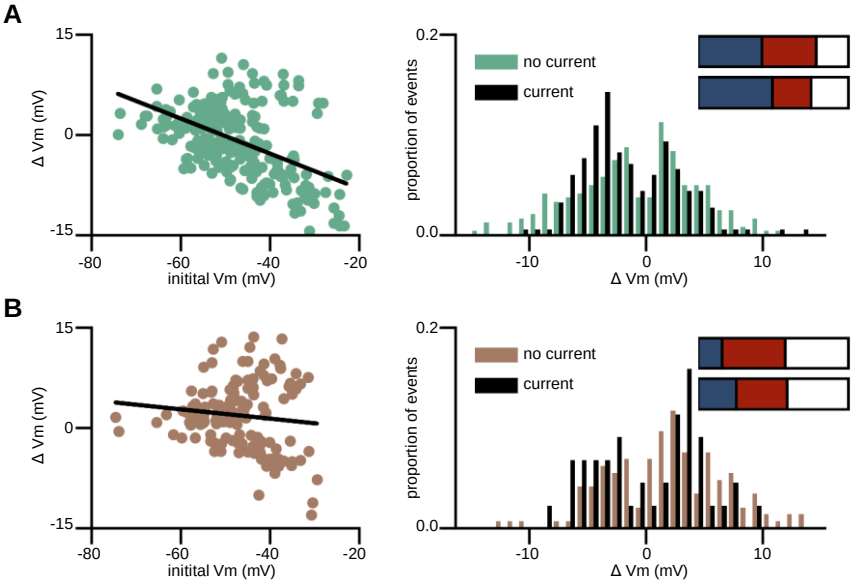
A
15
0
-15
Δ Vm (mV)
-80
-60
-40
-20
initital Vm (mV)
0.2
0.0
proportion of events
no current
current
-10
0
10
Δ Vm (mV)
B
15
0
-15
Δ Vm (mV)
-80
-60
-40
-20
initital Vm (mV)
0.2
0.0
proportion of events
no current
current
-10
0
10
Δ Vm (mV)

Figure 6 - Resting membrane potential influences the intracellular modulation of CA3 PCs during brain states. (A) Left: Vm changes during theta (ΔVm) versus the initial resting membrane potential (initial Vm) of the cell. Black solid line shows corresponding linear regression ($r = -0.46$, $p = 2.21 \times 10^{-14}$). Right: distribution of the changes in Vm during theta for events when no holding current was injected in the cell (no current) and when negative current was applied (current). Inset: bar charts of percent event type (hyperpolarizing, depolarizing, or no change) for theta events occurring during no current (top) and negative current (bottom) conditions. All types of events occurred at a similar frequency regardless of the injected current ($p=0.118$ for hyperpolarizing, $p=0.057$ for depolarizing, $p=0.273$ for no change). (B) Left: Vm changes during LIA (ΔVm) versus the initial resting membrane potential (initial Vm) of the cell. Black solid line shows corresponding linear regression ($r = -0.12$, $p = 0.16$). Right: distribution of the changes in Vm during LIA for events when no holding current was injected in the cell (no current) and when negative current was applied (current). Inset: bar charts of percent event type (hyperpolarizing, depolarizing, or no change) for LIA events occurring during no current (top) and negative current (bottom) conditions. All types of events occurred at a similar frequency regardless of the injected current ($p=0.078$ for hyperpolarizing, $p=0.754$ for depolarizing, $p=0.508$ for no change).

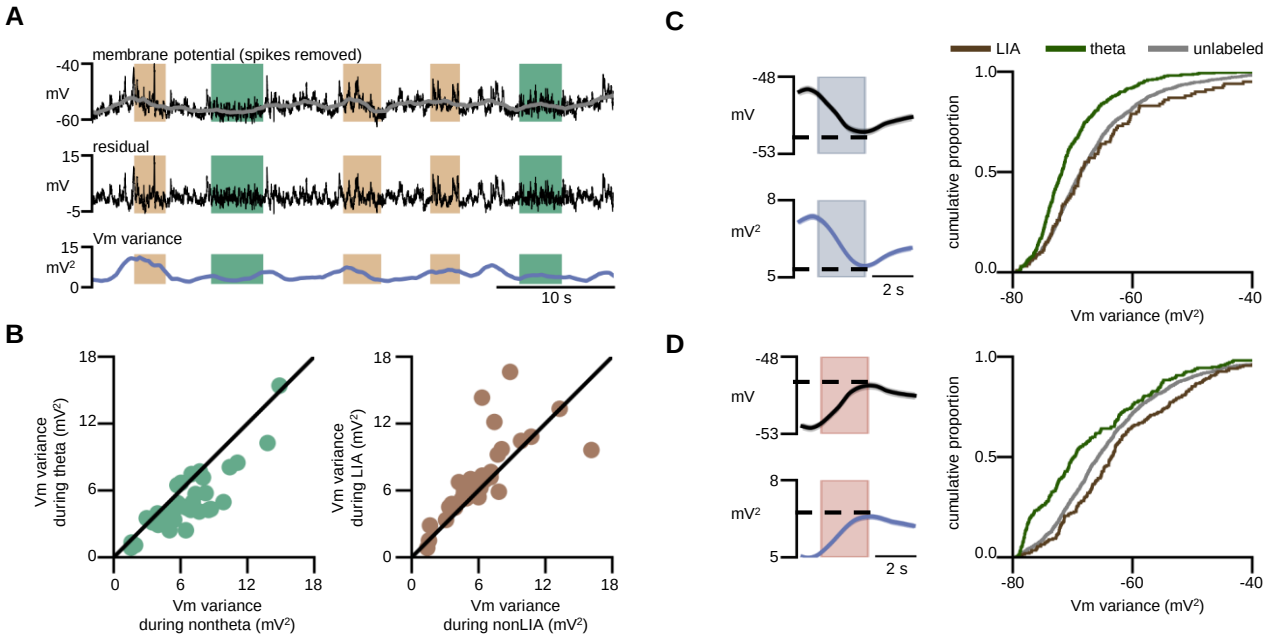
A
membrane potential (spikes removed)
-40
mV
-60
residual
15
mV
-5
Vm variance
15
mV²
0
10 s
B
Vm variance during theta (mV²)
Vm variance during nontheta (mV²)
Vm variance during LIA (mV²)
Vm variance during nonLIA (mV²)
0
6
12
18
C
-48
mV
-53
8
mV²
5
2 s
LIA
theta
unlabeled
cumulative proportion
1.0
0.5
0.0
-80
-60
-40
Vm variance (mV²)
D

Figure 7 - Variance of membrane potential of CA3 PCs is differentially modulated during theta and LIA. (A) Processing of Vm trace to measure its variance. Top: downsampled Vm after spike removal of a CA3 PC with shading indicating theta (green) and LIA (brown). The grey superimposed trace is after smoothing with a window of 2 seconds. The smoothed Vm is subtracted from the spike-removed Vm to obtain the residual Vm (middle). The variance of the residual Vm trace is calculated over 1-second windows (bottom). (B) Left: scatter plot showing Vm variance of each cell during theta versus nontheta (n = 35 cells). Filled dots represent a significant difference. Over the population of cells, there was a significant decrease in variance during theta (6.09 ± 2.21 mV^2 for nontheta, 4.33 ± 1.86 mV^2 for theta, mean difference = -1.58 mV^2, $p < 0.001$). Right: same as above but for LIA. Over the population of cells, there was a significant increase in variance during LIA (5.89 ± 2.15 mV^2 for nonLIA, 6.32 ± 2.42 mV^2 for LIA, mean difference = 0.96 mV^2, $p = 0.004$). (C) Left: Average of all hyperpolarizing events Vm (top, black) and variance (bottom, blue, n = 1945 events). Dotted line corresponds to the value taken at the end of the change in Vm for each event. Right: Cumulative proportion of variance during LIA (brown), theta (green) and unlabeled (grey) hyperpolarizing events. Vm variance is lower during theta, but there is no difference in Vm variance between LIA and unlabeled hyperpolarizations (3.29 ± 1.82 mV^2 [n = 421 events] for theta, 4.55 ± 3.20 mV^2 [n = 101 events] for LIA, 4.62 ± 2.74 mV^2 [n = 1426 events] for unlabeled, $p < 0.001$ for theta vs unlabeled and theta vs LIA, $p = 0.832$ for LIA vs unlabeled). (D) Left: Average of all depolarizing events Vm (top, black) and variance (bottom, blue, n = 2054 events). Dotted line corresponds to the value taken at the end of the change in Vm for each event. Right: Cumulative proportion of variance during LIA, theta and unlabeled depolarizing events. Vm variance is lower during theta, and higher during LIA when compared with unlabeled depolarizing events (4.22 ± 3.51 mV^2 [n = 219 events] for theta, 6.72 ± 3.64 mV^2 [n = 208 events] for LIA, 5.83 ± 3.51 mV^2 [n = 1631 events] for unlabeled, $p < 0.001$ for theta vs unlabeled and theta vs LIA, $p = 0.008$ for LIA vs unlabeled).